International Journal of Applied Earth Observation and Geoinformation 144 (2025) 104855

Contents lists available at ScienceDirect

International Journal of Applied Earth Observation and Geoinformation

journal homepage: www.elsevier.com/locate/jag

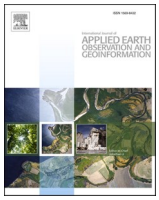

TerrainFloodSense: Improving seamless flood mapping with cloudy satellite imagery via water occurrence and terrain data fusion

Zhiwei Li [a,b,e], Shaofen Xu [a,d], Qihao Weng [a,b,c,*]

[a] JC STEM Lab of Earth Observations, Department of Land Surveying and Geo-Informatics, The Hong Kong Polytechnic University, Hung Hom, Hong Kong
[b] Research Centre for Artificial Intelligence in Geomatics, The Hong Kong Polytechnic University, Hung Hom, Hong Kong
[c] Research Institute for Land and Space, The Hong Kong Polytechnic University, Hung Hom, Hong Kong
[d] Department of Civil and Environmental Engineering, The Hong Kong Polytechnic University, Hung Hom, Hong Kong
[e] Department of Civil, Urban, Earth, and Environmental Engineering, Ulsan National Institute of Science and Technology, Ulsan, South Korea

ARTICLE INFO

Keywords:
Flood mapping
Cloud reconstruction
Data fusion
Harmonized Landsat and Sentinel-2 (HLS)
Extreme floods
Cloudy and rainy environments

ABSTRACT

Extreme flood disasters are intensified by climate change, exposing an increasing share of the global population to flood hazards. Accurate monitoring of inundation extents during floods is crucial for disaster management and impact assessment. While remote sensing can provide strong support for flood monitoring, optical satellite images often face significant challenges due to weather conditions and infrequent revisits, particularly in cloudy and rainy regions. To address this limitation and achieve seamless flood mapping with cloudy satellite images, this paper proposes TerrainFloodSense, a novel method that fuses water occurrence with terrain data to enhance the reconstruction of cloud-covered flooding areas, especially under extreme and unprecedented flood scenarios. Specifically, TerrainFloodSense first generates enhanced water occurrence data by Bayesian fusion of terrain indices, including Digital Surface Model (DSM) along with Height Above the Nearest Drainage (HAND), and historical water occurrence data. Then, enhanced water occurrence data are used to fill gaps caused by clouds in water maps derived from optical satellite images, guided by the submaximal stability assumption. The basic idea is that prior terrain information can be incorporated into the initial water occurrence data to enhance the ability to predict the inundation probabilities for both regular pre-flood water and extreme floodwater and to help reconstruction of cloud-covered flooding areas even under extreme flooding scenarios. Simulated experiments and applications in large-area flood mapping cases confirmed that TerrainFloodSense significantly outperformed existing methods, achieving absolute accuracy improvements of 2.95%–8.86% in overall accuracy and 0.038–0.087 increases in F1-Score under extreme flooding scenarios. This study demonstrated that the fusion of water occurrence and terrain data can effectively improve seamless flood mapping by using optical satellite images, supporting disaster monitoring and impact assessment in cloudy and rainy environments. The code associated with this study has been made publicly accessible via https://github.com/RCAIG/TerrainFloodSense.

1. Introduction

As one of the most common and severe natural disasters, floods have been intensified due to climate change, putting a larger proportion of the population at risk than ever (IPCC, 2023; Rentschler et al., 2022; Tellman et al., 2021). Obtaining timely flood information, such as extent and duration, is crucial for flood disaster emergency response and impact assessment, given the increasing flood risks (Li et al., 2024a,b,c). As two typical and low-cost ways for flood monitoring, satellite remote sensing and ground simulation and modeling have been widely used in different scenarios because of their respective strengths and limitations.

Satellite remote sensing can provide wide-range and direct observations of floods. Time series imagery from multiple satellites can be used to detect extents of surface water bodies and track their dynamic changes over time (Li et al., 2021b; Li et al., 2022; Yue et al., 2023). Flood inundated areas can then be highlighted and separated from regular inundated areas by excluding pre-flood water areas (Hashemi-Beni and Gebrehiwot, 2021; Chen et al., 2024). However, limitations in satellite-based flood monitoring primarily arise from two commonly used image sources, i.e., optical satellites and synthetic aperture radar

* Corresponding author at: JC STEM Lab of Earth Observations, Department of Land Surveying and Geo-Informatics, The Hong Kong Polytechnic University, Hung Hom, Hong Kong.
E-mail address: qihao.weng@polyu.edu.hk (Q. Weng).

https://doi.org/10.1016/j.jag.2025.104855
Received 31 March 2025; Received in revised form 27 August 2025; Accepted 13 September 2025
Available online 19 September 2025

(SAR) imagery (Konapala et al., 2021; Martinis et al., 2022). On the one hand, while there are relatively abundant data sources for optical satellite images, such as MODIS, Landsat and Sentinel-2, they are inevitably affected by cloud cover, which reduces their availability and valid observation frequency (Goffi et al., 2020; Li et al., 2021a; Li et al., 2022b; Shastry et al., 2023). On the other hand, SAR imaging is weather- and time-independent, making it an ideal data source for flood monitoring during adverse weather, such as cloud cover or rainfall. However, the limited open-access data sources for SAR images prevent their wider applications compared to optical satellite data. Additionally, the long revisits (e.g., 6–12 days for Sentinel-1) of SAR satellites make capturing short-duration flood events challenging (Helleis et al., 2022; Fichtner et al., 2023). Moreover, the heavy speckle noises in SAR images limit its effectiveness in complex urban areas (Notti et al., 2018; McCormack et al., 2022; Tupas et al., 2023), whereas optical satellite images can provide high-resolution surface details. Given the above facts, it is clear that the potential of satellite remote sensing for flood monitoring is significantly limited by cloud cover; thus, achieving seamless flood monitoring beyond clouds is crucial for leveraging optical satellite images to identify inundated areas. While our recent study (Li et al., 2024a) provided an initial solution to deal with this issue, the limitation under extreme flooding scenarios, such as one-in-hundred-year floods, necessitates further improvements.

Ground simulation and modeling methods focus on simulating inundation situations by modeling rainfall, runoff, and other hydrological processes across landscapes (Fraehr et al., 2023; Giustarini et al., 2016; Zingaro et al., 2024). The advantages of these methods lie in their ability to provide time-intensive simulated flood inundation information, even for areas with sparse observation data (Peramuna et al., 2025). Additionally, they can be used to simulate complex scenarios and predict flood inundation and risks under varied conditions, such as future climate scenarios (Fraehr et al., 2023; Tupas et al., 2023). However, limitations of these methods arise from their high dependence on data quality, such as terrain data, precipitation, and land cover (Schumann et al., 2022; Zingaro et al., 2024). Furthermore, they may require significant computational resources for high-resolution flood modeling, which reduces their efficiency in large-area flood inundation simulation (Wang et al., 2024b). While recent efforts have been made to boost flood simulation efficiency by using machine learning techniques (Yokoya et al., 2022; Fraehr et al., 2023; Xu et al., 2024), uncertainties in simulated inundation maps remain. These unavoidable uncertainties necessitate the combination of ground simulation and modeling with real observations, such as those obtained from satellites.

Considering the challenges in seamless flood mapping under clouds and the necessity of integrating ground simulation and satellite observations for enhanced flood mapping, we propose an effective method that fuses satellite and terrain data for enhanced seamless flood mapping. The development of the method is motivated by the limitations of previous studies in seamless flood mapping under extreme flooding scenarios (Tulbure et al., 2022; Li et al., 2024a). The effective reconstruction of cloud-covered flooding areas is subject to the availability of spatiotemporally neighboring satellite observations and the prior inundation probabilities based on auxiliary water occurrence data derived from historical satellite observations (Mullen et al., 2021; Martinis et al., 2022; Feng et al., 2023; Fichtner et al., 2023; Huang et al., 2023). Under extreme flooding scenarios, such as one-in-hundred-year floods, it remains particularly challenging to retrieve flood extent in areas obscured by cloud cover, especially those that have rarely or never been inundated in history and observed by satellites.

The basic idea of the proposed method lies in the fusion of water occurrence and terrain data, which can enhance the recovery of extreme flooding areas obscured by cloud cover. By directly fusing water occurrence and terrain data, rather than relying solely on computationally intensive terrain-based inundation simulation and modeling, the proposed method achieves spatially seamless flood mapping with significantly reduced computational costs. This innovative solution makes seamless flood mapping with cloud-covered optical satellite images effective even under extreme flooding scenarios.

While this study builds upon our previous work on seamless flood mapping using optical satellite image time series (Li et al., 2024a), it introduces substantial methodological advancements to address critical gaps in extreme flooding scenarios. The previous study primarily focused on leveraging spatiotemporal information from optical image series and ancillary water occurrence to reconstruct flood dynamics under general conditions. However, such an approach tends to be less effective in extreme flood events due to historical bias and uncertainty in the water occurrence data, particularly in regions with sparse or no prior inundation records. To overcome this limitation, this study introduces a terrain-informed Bayesian fusion framework that integrates terrain indicators, namely the Digital Surface Model (DSM) and Height Above Nearest Drainage (HAND), with historical water occurrence data, enabling more physically grounded flood susceptibility estimation. This allows for more robust reconstruction of flood extents in rarely inundated regions, where previous methods typically fail. Moreover, the proposed method is less dependent on spatiotemporal continuity of satellite observations, which is often disrupted during rapidly evolving or short-duration flood events. These improvements make the method developed in this study not merely an incremental extension, but a substantial advancement beyond our earlier work, particularly in terms of generalizability and applicability to extreme and unprecedented flooding conditions.

The key contributions of this study are outlined below:

1) We propose TerrainFloodSense, a novel seamless flood mapping method that significantly improves the accuracy of cloud reconstruction in inundation areas by fusing water occurrence and terrain data. Extensive experiments show that our method achieves absolute improvements in overall accuracy of 2.95 %–8.86 % under extreme flooding scenarios compared to benchmarks.
2) A simple but efficient Bayesian fusion framework is introduced that integrates historical satellite-derived water occurrence data with terrain-derived indices, i.e., DSM and derived HAND. This framework is applied to generate enhanced water occurrence, improving cloud reconstruction performances thereby benefiting seamless flood mapping.
3) This study highlights unignorable uncertainties in flood mapping caused by cloud cover effects and confirms the benefits of cloud reconstruction. Moreover, this study underscores the potential of TerrainFloodSense for seamless flood mapping to support emergency flood response and precise impact assessments.

With the goal of enhancing the spatial continuity and observation frequency in flood mapping, this study developed a novel method that leverages cloudy optical satellite images to achieve seamless flood mapping, thereby effectively complementing flood monitoring using SAR images alone. Particularly, the performance of seamless mapping under extreme flooding scenarios was improved via the fusion of water occurrence and terrain data. The solution developed in this study will effectively support disaster monitoring and impact assessment.

2. Study area and data

2.1. Study area

In this study, three flood events caused by heavy rainfall were selected for experiments and validation purposes. These three flood events were also selected because the corresponding regions are known for frequent exposure to flooding and widespread impacts (Rentschler et al., 2022; Tulbure et al., 2022). The geographic locations of the three study areas are shown in Fig. 1, and the flood event in each study area is representative of different hydrological and cloud-cover conditions. The three selected events are described below to highlight their distinct

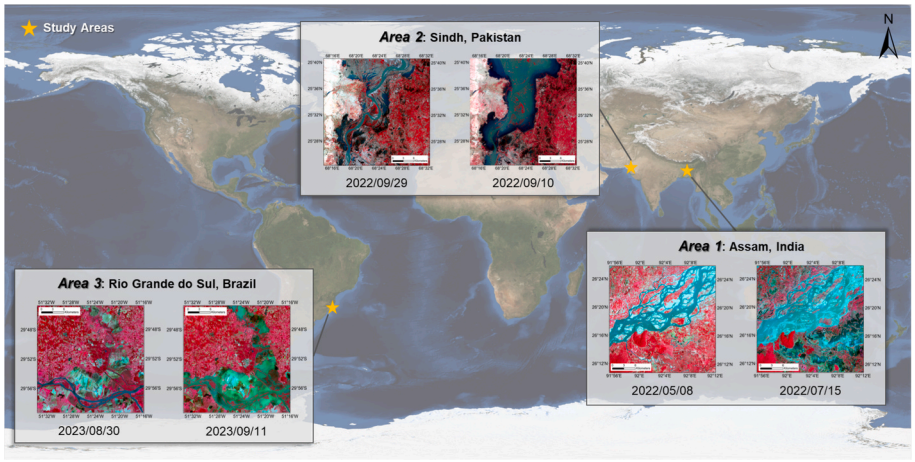

Fig. 1. Geographic locations of the three selected study areas for flood mapping (base map credit: NASA Visible Earth).

characteristics.

1) **Assam, India (May–August 2022)**: The first flood event occurred between May and August 2022 in Assam, India, a region situated along the Brahmaputra River and recognized as one of the most flood-prone areas globally due to monsoon-driven hydrology and low-lying terrain. This was a seasonal, monsoon-driven flood event, which is relatively regular given Assam's frequent and extensive flooding history.
2) **Sindh, Pakistan (August–September 2022)**: The second flood event took place in Sindh, Pakistan between August and September 2022, where widespread inundation and prolonged flood duration severely impacted agriculture and infrastructure, making it a critical region for evaluating large-area flood mapping performance. This was an extreme flood event triggered by exceptionally heavy rainfall, resulting in record-breaking impacts.
3) **Rio Grande do Sul, Brazil (September 2023)**: The third flood event occurred in Rio Grande do Sul, Brazil in September 2023, where intense rainfall led to river overflow. This was another extreme flood event caused by intense rainfall, exceeding historical flood levels in several areas that had rarely or never been previously inundated. Notably, this event was characterized by heavy cloud cover and infrequent satellite overpasses, making it an ideal case for evaluating cloud reconstruction and flood mapping methods.

2.2. Study data

The datasets used in this study cover all three study areas, and all have a 30-m resolution to ensure consistent data processing. The datasets include:

- Harmonized Landsat and Sentinel-2 (HLS): The HLS images (Claverie et al., 2018) were obtained from https://hls.gsfc.nasa.gov/. The HLS dataset combines observations from Landsat-8/9 and Sentinel-2 satellites, offering image acquisitions at intervals of 2–3 days. The HLS images obtained were used to derive initial water maps in this study, providing a reliable baseline for high-frequency flood monitoring.
- GSW Water Occurrence: Water occurrence data were collected from the Global Surface Water (GSW) dataset (Pekel et al., 2016), available at https://global-surface-water.appspot.com/download. The GSW dataset is generated based on 37-year Landsat observations from 1984 to 2021. In this study, the GSW water occurrence data will be used as ancillary input for seamless flood mapping.
- ALOS Digital Surface Model (DSM): The DSM data were sourced from the ALOS World 3D - 30 m (AW3D30) dataset (Tadono et al., 2014; Takaku et al., 2014), available at https://developers.google.com/earth-engine/datasets/catalog/JAXA_ALOS_AW3D30_V3_2. This DSM data is essential for identifying topographic depressions and low-lying flood-prone areas, which are critical for estimating potential inundation zones.
- Height Above Nearest Drainage (HAND): The HAND data were obtained from the Global 30 m Height Above the Nearest Drainage dataset (Donchyts et al., 2016), accessible via https://gee-community-catalog.org/projects/hand/. HAND represents the vertical distance from each pixel to the nearest drainage channel, and serves as a hydrological indicator of potential flood susceptibility, especially in areas lacking direct flood observations.

3. Methodology

To obtain seamless flood maps using optical satellite imagery, which are often affected by cloud cover, we proposed TerrainFloodSense, an improved method that reconstructs cloud-covered flooding areas by fusing terrain data with water occurrence derived from decades of satellite observations. As shown in Fig. 2, which takes the study area in Rio Grande do Sul, Brazil, as an example, TerrainFloodSense involves three key steps: data pre-processing, multi-source data fusion, and cloud reconstruction. The input data consists of HLS images, DSM data and derived HAND index, and GSW water occurrences, all with a 30-m resolution. The output is seamless flood maps in which regions masked by cloud cover in initial water maps are effectively reconstructed.

Specifically, the terrain data, i.e., DSM data and derived HAND data, were first normalized and combined to generate the terrain-derived inundation index; Then, the inundation index was fused with GSW water occurrence using the proposed Bayesian fusion framework to obtain enhanced water occurrence data. Finally, cloud reconstruction is applied to the initial water maps derived from HLS image series, using the enhanced water occurrence as ancillary data to fill the cloud-contaminated areas, in accordance with the submaximal stability assumption. The final seamless flood maps are produced by excluding pre-flood water areas from the reconstructed water maps. The details of the methodology are introduced in the following subsections.

3.1. Data preprocessing

The GSW water occurrence dataset indicates the frequency of water occurrence in a region based on decades of historical Landsat satellite observations, with occurrence percentages varying between 0 and 100. This dataset contains prior information on water dynamics and thus has been used as ancillary data to fill gaps caused by clouds in water maps

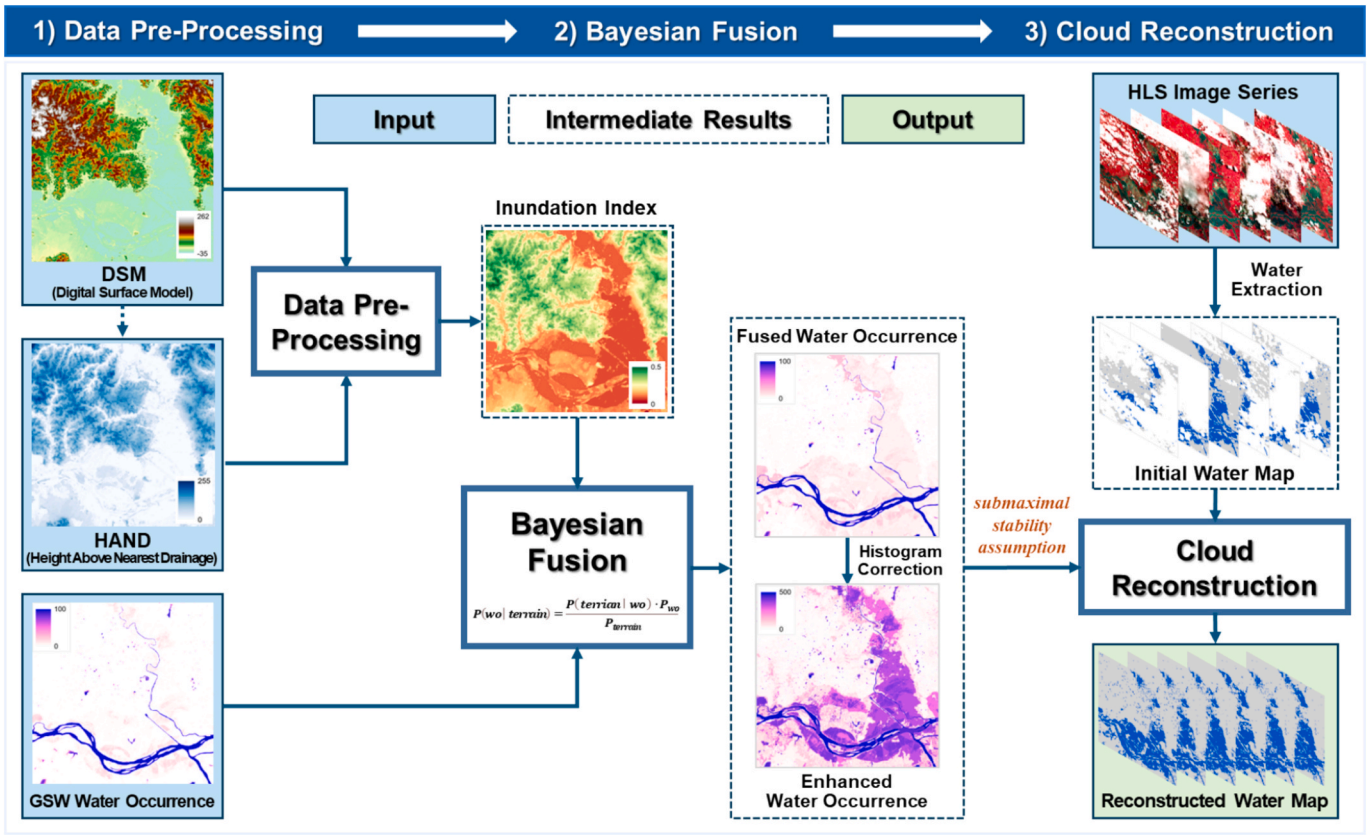

Fig. 2. Overview of TerrainFloodSense for seamless flood mapping from cloud-covered optical satellite imagery. The process comprises three main steps: (1) Data pre-processing and generation of terrain-derived inundation index maps; (2) Generation of enhanced water occurrence data through the fusion of GSW water occurrence and terrain data; and (3) Cloud reconstruction applied to cloud-contaminated areas in the initial water maps.

derived from cloudy Landsat images to obtain seamless water maps. However, limitations exist with the application of this dataset for seamless flood mapping, primarily in the following two aspects: **(1) Non-negligible uncertainties exist in low-occurrence water areas**, where short-term water dynamics, such as occasional floods, increase statistical biases due to limited observations. This problem is exacerbated under cloudy and rainy weather conditions when optical satellites fail to provide valid observations; **(2) Insufficient historical observations of extreme flood events** reduce the reliability of prior information contained in the water occurrence dataset for reconstructing the cloud-covered inundation areas. This issue becomes increasingly severe as climate change intensifies extreme flooding, causing areas rarely or never inundated in history to expand significantly.

To address these issues, this study integrates terrain data, i.e., DSM and HAND, to enhance the initial GSW water occurrence data and thus improve the cloud reconstruction for seamless flood mapping, especially under extreme flooding scenarios. Specifically, the DSM data were utilized to infer potential flood-prone areas. Given that susceptibility to floods is closely related to the proximity to drainage, the additional HAND index is employed to indicate the risk of specific areas being inundated. HAND represents the vertical distance between a given point and its nearest drainage location along the drainage network, and is computed as follows:

$$HAND = H_{pixel} - H_{drainage} \quad (1)$$

where H_{pixel} denotes the height of the target cell, and $H_{drainage}$ refers to the height of its nearest drainage location.

Generally, areas with lower elevation and closer proximity to drainage are more susceptible to flooding. The terrain-derived inundation index is computed as a weighted combination of the min–max normalized DSM and HAND indices.

$$Inundationindex = \alpha \bullet norm(DSM) + (1-\alpha) \bullet norm(HAND) \quad (2)$$

where α is a weighting coefficient that balances the contribution of the DSM and HAND indices to the inundation index; and *norm* refers to the min–max normalization operation.

In this study, α is empirically set to 0.3 based on sensitivity analysis, which enables a larger weight of 0.7 to be assigned to the HAND index as it provides more direct information on flood susceptibility. In the sensitivity analysis, we tested values of α ranging from 0 to 1 at 0.1 intervals across all three study areas, and evaluated the reconstructed flood maps against validation labels used for quantitative assessment in Section 5.1. Sensitivity analysis results indicated that $\alpha = 0.3$ achieved the best trade-off between precision and recall, with the highest overall accuracy. Thus, this value was adopted to balance the influence of DSM and HAND in identifying flood-prone areas. The obtained inundation index offers a more comprehensive representation of flood occurrence risk, especially for low-risk and potential future flooding regions. In addition, the two special cases where $\alpha = 0$ and $\alpha = 1$ can be regarded as ablation settings, where one terrain indicator (DSM or HAND, respectively) is excluded from the index. The results show that using either indicator alone yields suboptimal performance, confirming that both DSM and HAND contribute complementary information. Their fusion substantially improves the effectiveness of the terrain-derived inundation index in supporting subsequent cloud reconstruction for seamless flood mapping.

3.2. Generation of enhanced water occurrence data via multi-source data fusion

The GSW water occurrence quantifies the historical frequency of

surface water presence based on decades of Landsat satellite observations, capturing long-term water dynamics. Conversely, terrain-derived inundation index maps, calculated by combining DSM and the HAND index, encode prior knowledge of flood susceptibility based on terrain features. While these two datasets both describe inundation probability from different perspectives, they are fundamentally distinct. GSW water occurrence reflects the temporal frequency of surface water observed by Landsat satellites but lacks explicit terrain context, making it less sensitive to ephemeral inundation, such as short-term irrigation and floods. Conversely, the terrain-based inundation index encodes theoretically predicted flood inundation probability based on terrain features but without support from real observations.

Given the complementary nature of these two datasets, a Bayesian fusion framework is proposed to enhance GSW water occurrence data. Here, we define the fused water occurrence (FWO), denoted as P_{fwo}, as the posterior probability of water presence given the terrain-based inundation probability. Then P_{fwo} can be formulated as the equation below based on Bayes' theorem:

$$P_{fwo} = P(wo|terrain) = \frac{P(terrain|wo) \bullet P_{wo}}{P_{terrain}} \tag{3}$$

where $P(wo|terrain)$ is the posterior probability of water occurrence given terrain conditions, i.e., the fused water occurrence; $P(terrain|wo)$ is the likelihood function, describing the probability of a certain terrain condition given a historical water occurrence; and P_{wo} and $P_{terrain}$ represent the prior probability and marginal probability, respectively, indicated by the GSW water occurrence and terrain-derived inundation index.

In this study, in order to model P_{fwo} as the probability of water presence, and due to the limited availability of direct flood observations, we approximate $P(terrain|wo)$ based on $P(terrain|inundation)$, where *inundation* represents historical occurrences of water. Additionally, since P_{wo} falls within the normalized interval [0, 1] after normalization, the likelihood function $P(terrain|inundation)$ can be estimated based on the distribution of historical water occurrence P_{wo}. To ensure consistency and computational efficiency, this study estimates $P(terrain|inundation)$ using the statistical frequency analysis over historical inundation regions as indicated by P_{wo}. Although P_{wo} is used to identify inundation-prone areas, we do not directly model $P(terrain|wo)$. Instead, we use the regions indicated by water occurrence to sample terrain distributions, thereby approximating the likelihood of terrain given inundation. This strategy provides a practical and data-driven estimation of flood-conditioned terrain features, especially in scenarios where direct flood observation is sparse or unavailable.

Specifically, for each unique terrain condition h in inundation index map, the probability that regions with $P_{terrain} = h$ is associated with inundation is computed as:

$$P(terrain = h|inundation) = \frac{\sum P_{wo}(terrain = h)}{\sum P_{wo}} \tag{4}$$

where $P_{wo}(terrain = h)$ denotes the historical water occurrence of pixels where $P_{terrain} = h$. The denominator $\sum P_{wo}$ normalizes the probability by summing water occurrences.

This approach ensures that the likelihood estimation reflects flood inundation susceptibility while simplifying computation and preserving spatial variability across different topographic conditions. Instead of constructing full probability distributions, the likelihood function is stored as a precomputed lookup table of terrain-conditioned inundation probabilities, making the Bayesian fusion efficient and scalable.

With the estimated likelihood function, the FWO at each unique terrain condition h can be computed as:

$$P_{fwo}(inundation|terrain = h) = \frac{P(terrain = h|inundation) \bullet P(inundation)}{P(terrain = h)} \tag{5}$$

where $P(terrian = h|inundation)$ is derived from Eq. (4); $P(inundation)$ and $P(terrain = h)$ denotes the general inundation probability and inundation probability under certain terrain condition h, respectively, which are defined as:

$$P(inundation) = \frac{\sum P_{wo}}{\sum P_{wo} + \sum (1 - P_{wo})} \tag{6}$$

$$P(terrain = h) = \frac{\sum P_{wo}(terrain = h) + \sum (1 - P_{wo}(terrain = h))}{\sum P_{wo} + \sum (1 - P_{wo})} \tag{7}$$

With Eqs. (4)–(7), the FWO under certain terrain conditions can be obtained with the simplified equation below:

$$P_{fwo}(inundation|terrain = h) = \frac{\sum P_{wo}(terrain = h)}{\sum P_{wo}(terrain = h) + \sum (1 - P_{wo}(terrain = h))} \tag{8}$$

The simplified Eq. (8) indicates that the FWO under certain terrain conditions can be approximated by computing their average water occurrences. Such an averaging water occurrence operation for each unique terrain conditions doesn't require considering the absolute values of the inundation index $P_{terrain}$, instead, it consider only specific terrain conditions by dividing $P_{terrain}$ into subregions with unique values. Additionally, the precomputed lookup table of terrain-conditioned inundation probabilities enables the effective fusion of the water occurrence data and terrain data. In summary, the Bayesian fusion framework, as represented by Eq. (3), and approximate estimation of FWO based on Eqs. (4)–(7), provide theoretical support for the simplified but effective estimation of FWO under different terrain conditions according to Eq. (8).

To balance FWO with original GSW water occurrence, the generated FWO is mean–variance normalized to the [0,1] range, followed by a weighted combination with P_{wo} as follows:

$$P_{fwo}^{final} = \alpha P_{fwo} + (1 - \alpha) P_{wo} \tag{9}$$

where α is a weighting coefficient that controls the contribution of the FWO relative to the initial GSW water occurrence dataset. An empirical setting of 0.5 for α ensures a neutral balance between model-inferred and observation-based water occurrence components, reducing the risk of overfitting to either source, especially under varying regional hydrological contexts.

Note that the Bayesian fusion is restricted to areas exhibiting significant uncertainties in the GSW water occurrence dataset, empirically defined as regions with water occurrence values below 5. The threshold of 5 is chosen with reference to previous studies (Feng et al., 2023; Li et al., 2021a; Wang et al., 2024a) and serves as a conservative criterion to capture underdetected flood areas without overly disturbing stable water body representation. This strategy ensures corrections are made only where necessary while preserving reliable estimates in the GSW water occurrence data. With the aim of further refining the FWO and maintain statistical consistency, histogram matching is applied between the FWO and initial GSW water occurrence data. Since terrain data introduces finer variability, the fusion process may increase the number of unique values, potentially reducing stability in subsequent analyses. Histogram matching mitigates this issue by aligning the statistical distribution of the FWO with the initial GSW water occurrence, ensuring interpretability while incorporating terrain constraints. Additionally, to better capture subtle variations in water occurrence, the final enhanced water occurrence data is discretized into 500 levels, compared to the original 100 levels. This increase in quantitative levels allows for a more precise representation of water occurrence.

After applying all the above processing steps, the final output is referred to as the enhanced water occurrence (EWO), denoted as P_{ewo}, which integrates both satellite-derived and terrain-based information,

ensuring improved accuracy and reliability for subsequent cloud reconstruction processing.

3.3. Reconstruction of missing regions in water maps

Following the water extraction and cloud reconstruction methods introduced in our previous study (Li et al., 2024a), and with the use of the EWO dataset, improved seamless flood maps can be obtained based on initial water maps generated using the HLS image time series. Specifically, we conducted high-accuracy water extraction based on HLS images using the fine-tuned Prithvi-100M-Sen1Floods11 model (Jakubik et al., 2023). This model is a transformer-based deep learning architecture pretrained on HLS datasets using the masked autoencoding strategy, and it has demonstrated strong generalization across different geographic and seasonal conditions. In this study, it was applied to generate water maps from HLS images for flood mapping. The generated water maps are overlaid with cloud masks extracted from HLS quality band to mask out invalid areas due to cloud cover.

These invalid areas caused by clouds and cloud shadows in initial water maps are then reconstructed using binary segmentation of the EWO data with a confidence threshold that is adaptively determined based on the submaximal stability assumption (Li et al., 2024a). This assumption is grounded on three key observations: (1) water under regular conditions often falls within the range of maximum observed extents; (2) water dynamics typically occur in areas with low historical occurrence; and (3) cloud cover has a stronger effect on the detection confidence of low-occurrence water pixels. Based on this assumption, a ratio curve is constructed from the pixel count distributions of water occurrence across cloud-free and inundated areas. This curve serves as a relative confidence indicator for water presence at different occurrence levels. Accordingly, threshold values associated with high-confidence levels are determined to assist in filling gaps caused by clouds in the initial water maps. Nonetheless, while prior terrain information is incorporated into the EWO, it also introduces unwanted noise. This noise is primarily due to artifacts in the underlying terrain data (e.g., DEM irregularities or HAND inaccuracies), and inconsistencies between the spatial patterns of terrain variables and the water occurrence data. To mitigate these effects, the derived ratio curve is smoothed using a moving-window average filter before being used to determine the optimal threshold for reconstruction.

The reconstruction process was performed iteratively using a local sliding window, progressively processing each pixel and image, as described in our previous study (Li et al., 2024a). Cloud-covered regions within water maps were categorized into water (1) or non-water (0) classes based on the threshold-based segmentation of EWO. The segmentation process is expressed as follows:

$$W(x,y) = \begin{cases} 1, \text{if } P_{ewo}(x,y) > T \\ 0, \text{otherwise} \end{cases} \tag{10}$$

where $P_{ewo}(x,y,t)$ denotes the enhanced water occurrence of pixel (x,y), and T is the optimal segmentation threshold determined within a localized window centered on the target location.

Specifically, the segmentation threshold is adaptively determined on a per-pixel basis using a localized sliding window. For each cloud-covered pixel, the optimal threshold is computed by analyzing the distribution of EWO values within the surrounding window. If the number of valid neighboring pixels is insufficient, the window size is progressively expanded until a reliable estimate can be made. This multi-scale sliding window strategy enables the method to accommodate local variability and spatial heterogeneity in water occurrence patterns. In cases where a stable local threshold cannot be determined, such as in highly noisy or sparsely observed regions, a fallback global threshold derived from the overall ratio distribution is applied to ensure robustness.

In line with previous studies (Zhao and Gao, 2018; Mullen et al., 2021), cloud-covered areas with water occurrence values above the determined threshold are assumed to be inundated; otherwise, they are not. This assumption enables the effective reconstruction of potential flooding regions obscured by clouds or lacking valid observations. The seamless flood map is finalized after reconstructing cloud-covered regions in the initial maps. Additionally, flood-inundated areas are extracted by subtracting water extents observed prior to the event, which represent maximum extent of water before the flooding event and are derived from pre-flood HLS imagery. Consequently, the final flood maps include three classes, i.e. floodwater, pre-flood water, and non-water.

4. Compared methods

Two methods were used for performance evaluation and comparison with the developed reconstruction method in this work. One of them is the representative reconstruction method developed by Zhao and Gao (2018), which employs GSW water occurrence as auxiliary data to fill gaps caused by clouds in water maps derived from contaminated images. In addition, the method proposed in our previous study (Li et al., 2024a), specifically developed for seamless flood mapping using HLS images and GSW water occurrence data, was also compared. Notably, the results by Li et al. (2024a) were obtained after cloud reconstruction but without applying time-series refinement of water maps, to ensure a fair comparison. Furthermore, unlike the two compared methods that rely on the original GSW water occurrence, the proposed method in this study utilizes the enhanced water occurrence (EWO) as its core input.

5. Results

5.1. Quantitative assessment of reconstructed flood maps

To assess the quantitative improvements achieved by TerrainFloodSense for seamless flood mapping using the generated EWO data, we conducted a series of simulated data reconstruction experiments on the three flood events. Specifically, cloud-free patches with sizes of 1000×1000 pixels (900 km^2) from HLS images during both flood and non-flood periods (i.e., before/after floods) were selected from each study site. In this study, six HLS images from the three study sites were used in simulated data experiments. The corresponding reference water maps for the six HLS images were manually labeled with high confidence through visual interpretation of cloud-free HLS image patches, assisted by high-resolution satellite imagery (e.g., Sentinel-2 and PlanetScope when available), and validated using local flood reports and expert hydrological knowledge. These labeled maps served as reference data for validating the accuracy of the reconstructed flood maps. To comprehensively simulate varying conditions of cloud cover, three cloud cover conditions were defined based on cloud percentages: low (less than 30 %), medium (between 30 % and 60 %), and high (greater than 60 %). For each cloud cover condition, four real cloud masks with varying cloud distributions were randomly generated from the quality assessment band of cloudy HLS images after appropriate resampling and cropping operations. These real cloud masks were subsequently overlaid with each reference water map of the three study sites, resulting in cloud-contaminated water maps for reconstruction. Consequently, there were 72 groups of simulated reconstruction experiments under three different combinations of cloud coverage levels and flood scenarios for the three flood events. All simulated cloud-covered water maps under varying cloud coverage levels are provided in Fig. A1 of Supplementary materials.

Note that the EWO primarily enhances GSW water occurrence (WO) in areas characterized by infrequent water presence, which are likely to be inundated during extreme flood events, particularly in regions where flood inundation has rarely or never been observed. In contrast, EWO remains consistent with the original WO in regions with consistently high water presence, including permanent and seasonal water bodies.

Therefore, in addition to performing accuracy evaluations on the entire water map, we divided the areas within each water map into two scenarios—regular inundation and extreme flooding—to comprehensively evaluate the performance of different methods. Specifically:

- **Extreme flooding areas** are defined as rarely inundated areas with GSW water occurrence values below 5, including areas inundated during the studied flood events but never effectively observed by Landsat satellites historically (indicated by a GSW water occurrence value of zero). Here, inundated areas in the flood events studied are represented by the composed maximum water extent map based on time series HLS images during the flood period.
- **Regular inundation areas** are defined as regions in the water map excluding the extreme flooding areas defined above. Water dynamics in the regular inundation areas are normally caused by seasonal or long-term changes, whereas short-term inundation or infrequent water dynamics typically occur in extreme flooding areas.

Thus, three scenarios were designed for accuracy evaluations of different methods: overall, extreme flooding, and regular inundation. To quantitatively evaluate accuracy, the outputs of different reconstruction methods were validated using the reference water maps. Five metrics were used, including overall accuracy (OA), precision, recall, mIoU, and F1-Score. Table 1 provides detailed quantitative evaluation results of different methods, where the mean accuracies under each scenario are calculated based on 72 groups of simulated data experiments. Additionally, detailed accuracy evaluation results under varying cloud cover conditions are provided in Table A1 of supplementary materials. Results from overall scenarios show that TerrainFloodSense incorporating EWO achieves net gains of 1.24 % and 0.024 with respect to OA and F1-Score compared to our method using WO, and larger improvements of 5.31 % and 0.086 compared to the method of Zhao and Gao (2018), respectively. These improvements are further illustrated in Fig. 3, where seamless flood maps reconstructed by different methods are compared against ground truths to reveal differences in commission and omission errors. It is evident that our method using EWO yields fewer reconstruction errors than the other two baseline approaches. Moreover, the proposed method demonstrated substantial improvements over the two compared methods in the extreme flooding scenario, with absolute increases of 2.95 %–8.86 % in overall accuracy and 0.038–0.087 in F1-Score. Also, the proposed method exhibited moderate improvements in the regular inundation scenario, with absolute increases of only 0.48 %–3.57 % in overall accuracy and 0.011–0.076 in F1-Score.

Notably, although Zhao and Gao (2018) demonstrate higher recall across all scenarios, this is primarily due to their global thresholding strategy, which tends to over-include uncertain pixels, especially in flood-prone areas with low GSW water occurrence values. While this method enhances recall, it also leads to lower precision, particularly under extreme flooding conditions. By contrast, our method leverages EWO to better differentiate true inundation from noise, resulting in a more balanced reconstruction, improving precision while maintaining acceptable recall. Consequently, our method achieves consistently higher OA, F1-scores, and mIoU, reflecting more reliable cloud reconstruction in flood mapping.

Generally, simulated data experiments demonstrate that prominent improvements in reconstruction accuracy brought by EWO primarily originate from the extreme flooding scenario, whereas improvements are less significant in regular inundation areas. These results are consistent with the motivation and expectation of the proposed method, which aims to enhance seamless flood mapping performance, particularly under extreme flooding scenarios, by using EWO data compared to methods using WO. Nevertheless, it should be noted that the performance of different methods in the overall scenario is dominated by performance under regular inundation conditions, because extreme flooding areas in the three tested regions are relatively small. However, improvements in the extreme flooding scenario are highly significant for flood mapping, especially when more severe flood disasters occur and dramatically increase inundation risks for areas that have never or rarely been inundated in history due to climate change.

5.2. Application of seamless mapping to large-area extreme floods

To further assess the performance of TerrainFloodSense for seamless mapping of large-area floods, we selected the entire tile of the HLS image acquired during the flood event that occurred in Rio Grande do Sul, Brazil, in 2023 for evaluation. Similarly, the initial water map was obtained by combining the cloud/shadow mask from the HLS quality band with the water extraction result generated by the fine-tuned Prithvi-100M-Sen1Floods11 model (Jakubik et al., 2023). This initial water map was then fed into our reconstruction methods using WO and EWO to obtain seamless flood maps, respectively. To visually assess the reconstructed results, we compared them against a 3-m resolution PlanetScope image collected on the same day as the HLS image (September 9, 2023). Due to an approximately one-hour gap in local time between the acquisition of the HLS and PlanetScope images, the cloud cover conditions varied between the two images, while flooding conditions were assumed to remain similar over such a short period. Certain areas covered by clouds in the HLS image but cloud-free in the PlanetScope image made it possible to visually validate the reconstructed flood maps using the PlanetScope image, despite cloud cover and partial data gaps existing in the PlanetScope image. Additionally, the NDVI map derived from the PlanetScope image, which effectively distinguishes inundated regions from non-water surfaces (Vermote and Saleous, 2007; Zhu and Woodcock, 2012), was also utilized to assist in validating inundated areas in the reconstructed flood maps. Although other indices like NDWI or combined metrics may enhance distinction, NDVI was selected for its simplicity and its strong spectral contrast between vegetation and water in high-resolution imagery. A visual comparison is shown in Fig. 4, where zoomed-in comparisons of local regions that were cloud-free in the PlanetScope image were conducted. Note that these visual

Table 1
Performance comparison of different cloud reconstruction methods for seamless flood mapping across varying flooding scenarios.

Scenarios	Method	Overall accuracy	Precision	Recall	mIoU	F1-score
Overall Scenario	Zhao and Gao (2018)	89.00 %	70.39 %	**90.58 %**	0.656	0.792
	Ours with WO	93.07 %	83.54 %	87.24 %	0.744	0.854
	Ours with EWO	**94.31 %**	**87.21 %**	88.36 %	**0.782**	**0.878**
Extreme Flooding	Zhao and Gao (2018)	80.78 %	75.86 %	**80.32 %**	0.640	0.780
	Ours with WO	86.69 %	91.20 %	75.99 %	0.708	0.829
	Ours with EWO	**89.64 %**	**95.42 %**	79.42 %	**0.765**	**0.867**
Regular Inundation	Zhao and Gao (2018)	92.88 %	70.16 %	**99.93 %**	0.701	0.824
	Ours with WO	95.96 %	81.81 %	97.51 %	0.801	0.890
	Ours with EWO	**96.44 %**	**84.46 %**	96.51 %	**0.820**	**0.901**

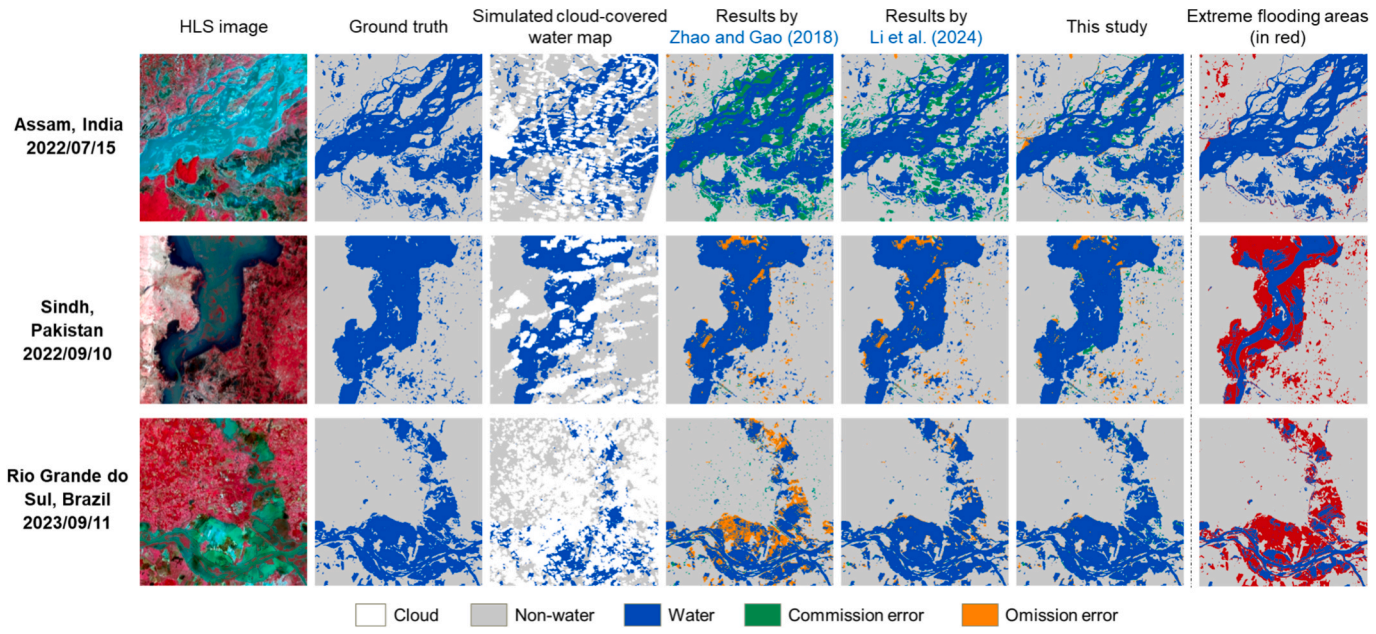

Fig. 3. Simulated data experiment results of the compared reconstruction methods for seamless flood mapping over local regions within the three study sites. Note that the outputs from the two baseline methods rely on the original GSW water occurrence, while those from the proposed method rely on the enhanced water occurrence. Moreover, the results by Li et al. (2024a) were obtained after cloud reconstruction but without applying time-series refinement of water maps to ensure a fair comparison. Extreme flooding areas, as defined in the context, are highlighted in red for distinction from regular inundation areas and are shown in the last column of the figure for reference. (For interpretation of the references to colour in this figure legend, the reader is referred to the web version of this article.)

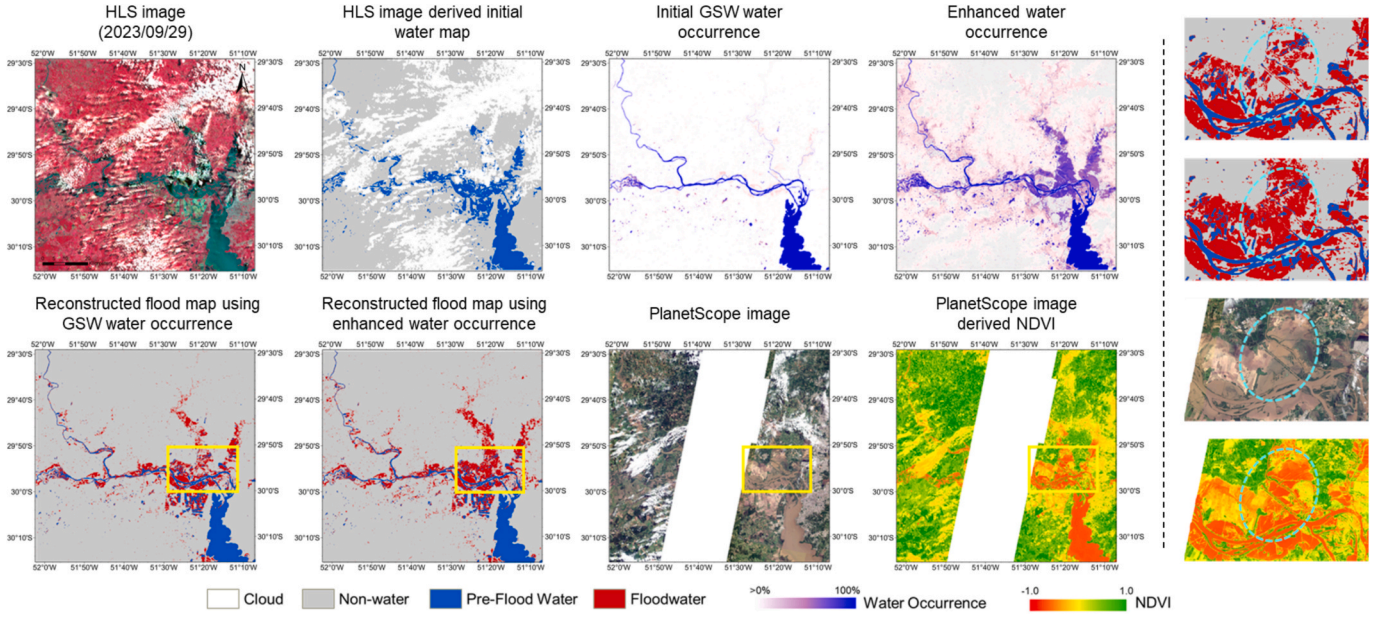

Fig. 4. Application of TerrainFloodSense for seamless flood mapping in Rio Grande do Sul, Brazil, on September 29, 2023, and comparisons using the PlanetScope image and derived NDVI. Note that the initial GSW water occurrence and the enhanced water occurrence were set at 100 and 500 levels, respectively, but were re-mapped to the same 0 %–100 % color range for visual comparisons. Areas exhibiting lower NDVI values typically indicate a greater probability of being inundated.

comparisons aim to qualitatively illustrate reconstruction performance at local scales, as large-area quantitative validation remains challenging due to the absence of consistent reference data. These comparisons further confirmed the accuracy and superiority of the reconstructed flood map produced using EWO compared to that produced using WO. Particularly, comparisons at two local regions highlighted improvements achieved by EWO in reconstructing cloud-covered inundation areas under extreme flooding scenarios.

6. Discussion

6.1. *Fusing multi-source data for extreme flood mapping*

Climate change is intensifying the frequency of extreme flood events, posing increased threats to human lives and infrastructure. Real-time flood mapping is critical for disaster response and post-flood management, but in situ data collection during flood events is often impractical. While satellite remote sensing offers a powerful solution, its

effectiveness is significantly constrained by cloud cover, which limits its usability for spatiotemporally continuous flood monitoring.

Cloud reconstruction has become essential for improving the continuity of flood mapping using optical satellite images. Existing reconstruction methods mostly rely on either historical water occurrence data (Zhao and Gao, 2018; Mullen et al., 2021) or spatiotemporal interpolation using cloud-free observations from neighboring dates (Bai et al., 2022; Huang et al., 2023). However, water occurrence data may be highly biased, as extreme floods are rarely observed historically. Moreover, water extents normally change dramatically and significantly during flood periods over short time scales, making accurate interpolation of cloud-covered inundation areas based on temporally adjacent observations challenging and unreliable. As a result, conventional WO-based methods often struggle to recover inundation areas obscured by clouds during extreme flood events.

Multi-source data fusion techniques are useful for addressing limitations inherent in single-source data (Albanwan et al., 2024). In this study, incorporating additional data containing prior terrain information can potentially improve extreme flood mapping. Publicly available datasets, including DSM, HAND indices, and global hydrological networks, provide valuable information for identifying flood-prone areas. Among them, elevation data has long been fundamental for hydrological analysis, offering indirect indicators of inundation probability, especially useful when valid satellite observations are unavailable. As demonstrated by the proposed method, the fusion of direct satellite observations with terrain-derived inundation probability data is a promising direction to enhance future flood mapping, particularly under extreme flooding scenarios.

In addition, combining SAR and optical imagery can be highly beneficial for improving flood mapping, particularly since SAR is not affected by cloud cover and provides consistent observations regardless of weather conditions (Martinis et al., 2022; Fichtner et al., 2023). Integrating SAR with optical time series could further enhance the temporal continuity and reliability of flood monitoring, especially during periods of persistent cloud cover (Li et al., 2024a). However, SAR data often suffers from speckle noise and shows reduced reliability in urban or densely vegetated areas. Moreover, due to differences in imaging mechanisms between SAR and optical sensors, inconsistencies may arise in the extracted water extents (Li et al., 2024a), highlighting the need for effective strategies to harmonize results from both data sources. Our method, which incorporates terrain-derived probabilistic priors, can complement SAR-optical fusion by guiding the reconstruction process where either data source alone may be insufficient. Moreover, airborne platforms such as UAVs offer valuable high-resolution data for local flood monitoring, assessment, and validation (Fawakherji and Hashemi-Beni, 2025; Li et al., 2025). These platforms can capture detailed inundation features that are often missed by satellite sensors. Nevertheless, their operational use is generally limited to small spatial extents and post-event scenarios due to cost, logistics, and coverage constraints. Therefore, while satellite data fusion offers an efficient solution for large-scale flood mapping, future research may benefit from exploring integrated frameworks that combine satellite, airborne, and in-situ data to improve accuracy and coverage, particularly in regions with complex hydrodynamics or human-made structures.

6.2. Benefits of cloud reconstruction for flood mapping

Currently available optical satellite data sources are more abundant than SAR data sources for flood monitoring, thus providing more frequent observational data, which, however, must overcome limitations imposed by cloud cover. Flood disasters occur mostly under cloudy and rainy weather conditions, making valid observations of large-area flood extents by optical satellites challenging. To leverage incomplete observational data for emergency flood mapping in support of disaster response and impact assessment, cloud reconstruction methods are urgently needed, especially when there are no other cloud-free optical satellite images or SAR images available. Both previous studies (Bai et al., 2022; Huang et al., 2023; Li et al., 2024a) and this study demonstrate that cloud reconstruction can significantly enhance the continuity of time series water or flood mapping with optical satellite images, even in cases with limited cloud-free observations. The benefit of cloud reconstruction for flood mapping lies not only in providing seamless flood maps but also in enhancing the accuracy of estimates of peak flood extents and flood durations, which are vital for post-disaster impact assessment (Bofana et al., 2022). Fig. 5 illustrates comparisons of flood duration maps of Rio Grande do Sul, Brazil, during the 2023 flood event composed with and without consideration of cloud cover effects. The comparisons underscore significant spatial inconsistencies and underestimation errors associated with flood duration maps composed without considering cloud cover effects, as highlighted by red circles. These issues arise due to gaps caused by clouds in time-series flood maps. Consequently, there will be non-negligible uncertainties in composed maximum flood extent and flood duration maps without considering cloud cover effects, which require attention when using optical satellite images for flood monitoring. Such issues necessitate cloud reconstruction to mitigate uncertainties in composed flood maps. Undoubtedly, cloud reconstruction benefits continuous flood observation, enabling better support for disaster management and impact assessment.

6.3. Limitations

Compared with previous cloud reconstruction or interpolation-based methods (e.g., Zhao and Gao, 2018; Bai et al., 2023), the proposed method offers notable advantages by fusing terrain information (DSM and HAND) with historical water occurrence. This fusion provides a physically-informed prior that supports more robust flood mapping, particularly under extreme flooding scenarios with sparse optical observations. In addition, the adaptive local thresholding strategy based on submaximal stability facilitates the accurate reconstruction of fine-scale inundation patterns that are often not recovered by conventional global or fixed-threshold approaches. Despite these strengths, several limitations related to the dataset and methodology remain and require further consideration.

First, the precision of the generated EWO data is subject to the quality of the DSM data used. Due to resolution constraints and inherent errors in the DSM dataset (ALOS DSM), uncertainties exist in the terrain data (Takaku et al., 2016). These uncertainties cause inconsistencies between inundation probabilities inferred from terrain data and the real inundation extent observed by satellites. Furthermore, such uncertainties introduce biases into the generated EWO data, subsequently reducing the reliability of reconstructed flood maps. To constrain these negative biases, the enhancement of water occurrence is only applied to areas exhibiting low water occurrence values that are likely to be inundated during extreme flood events. In our experiments, as shown in Fig. 6, one case illustrates that our proposed method may not perform well, particularly in regions lacking elevation details due to DSM data quality issues. To clearly identify areas where the EWO data contains substantial uncertainties, we overlaid the satellite-observed flood map on the visualized DSM, HAND, and EWO data. The locally inconsistent areas, where inundation was observed by satellites but EWO failed to indicate significant inundation probability, are highlighted by the yellow circle in Fig. 6. These inconsistencies between EWO and satellite-observed flood extents arise from DSM data uncertainties, as illustrated by the absence of significant elevation changes in inconsistent regions. This limitation of the proposed method can only be mitigated by using alternative DSM datasets with higher resolution and better quality.

Second, only two terrain indices, i.e., DSM and derived HAND, were involved in the fusion with water occurrence to generate EWO. While the proposed fusion of multi-source data effectively incorporates terrain and associated hydrological information into satellite observation-derived water occurrence data, it primarily considers statistical

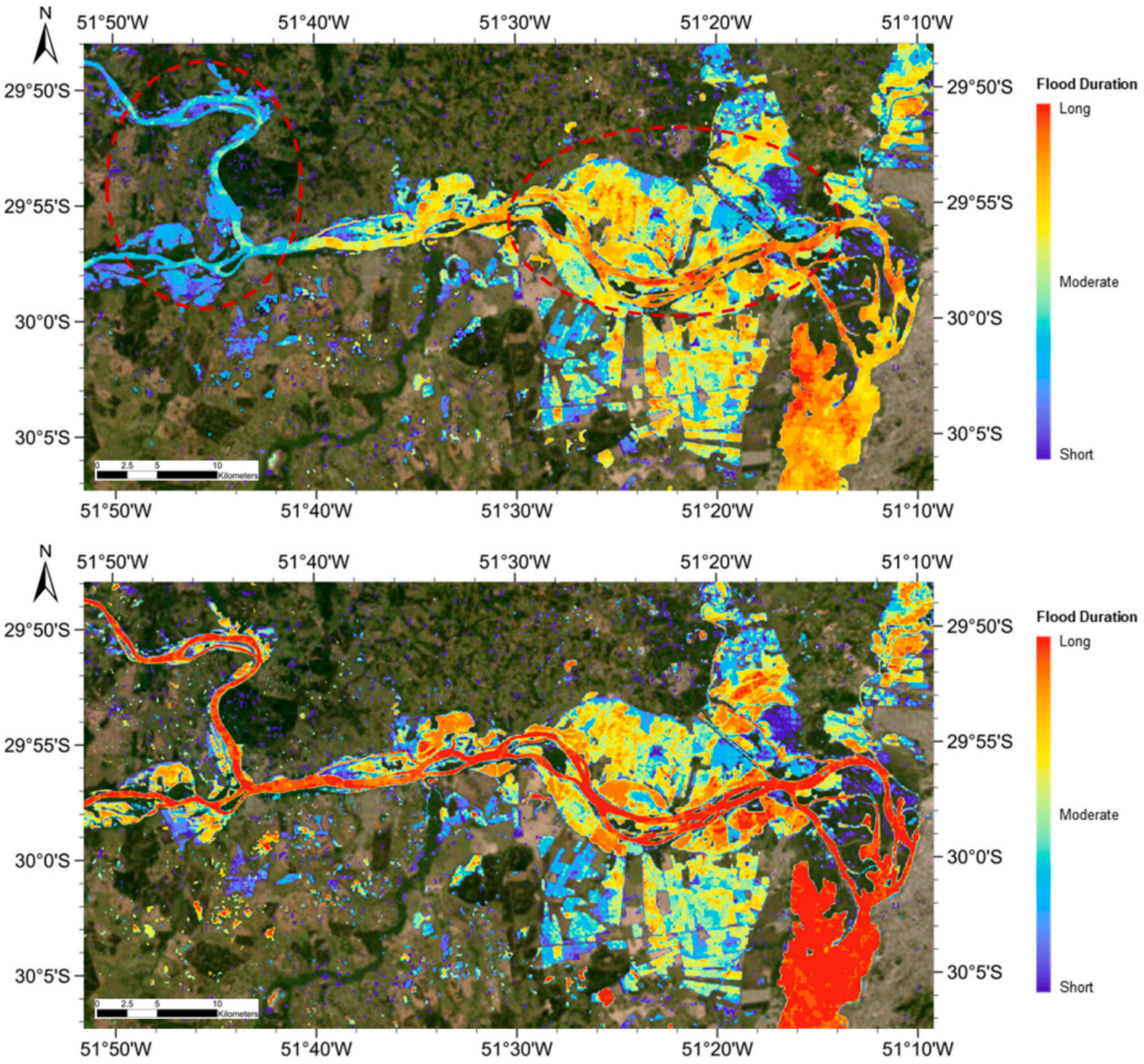

Fig. 5. Comparisons of satellite-estimated flood duration maps of Rio Grande do Sul, Brazil, during the 2023 flood event composed without (upper subfigure) and with (lower subfigure) considering cloud cover effects. Note that the flood duration maps were composed based on water maps derived from 21 HLS images collected from August 30 to November 6, 2023. Cloud cover in optical satellite image time series leads to significant spatial inconsistencies and underestimation errors in the composed flood duration map (upper subfigure). Cloud cover effects in the lower subfigure were effectively mitigated by applying cloud reconstruction to fill gaps caused by clouds in the time-series flood maps.

inundation probability priors without explicitly capturing complex hydrological and hydrodynamic processes. Generally, areas with lower elevations in DSM and lower HAND values exhibit higher flood susceptibility. However, exceptions exist in real-world conditions that do not align well with this general trend, such as areas with above-ground rivers or artificial structures. Such exceptions potentially introduce biases in the EWO data. Thus, while the proposed Bayesian fusion approach is effective, it requires further improvement through incorporation of local hydro-physical processes to achieve greater accuracy in seamless flood mapping.

7. Conclusions

Optical satellites can provide abundant data sources for flood monitoring, complementing SAR imagery and improving observation frequency. However, their useability is notably constrained by cloud cover, which necessitates the use of cloud reconstruction techniques to produce seamless flood maps for timely disaster response.

This study introduced TerrainFloodSense, an improved seamless flood mapping method that fuses historical water occurrence data with terrain indices (DSM and HAND) to enhance cloud reconstruction performance in extreme flood events. Both simulated experiments and applications confirmed the superiority of TerrainFloodSense, achieving absolute improvements of 2.95 %–8.86 % in overall accuracy and 0.038–0.087 in F1-Score under extreme flooding scenarios. Additionally, the proposed method maintained similar performance with benchmarks in regular inundation scenarios. Unlike the previous study (Li et al., 2024a), the proposed method reduces dependence on the spatiotemporal continuity of satellite observations and improves robustness in regions with sparse or no historical inundation records. These improvements validate the capability of TerrainFloodSense to support high-quality seamless flood mapping for future extreme events.

This study highlights the value of multi-source data fusion, particularly integrating satellite observations with terrain-derived indices, for

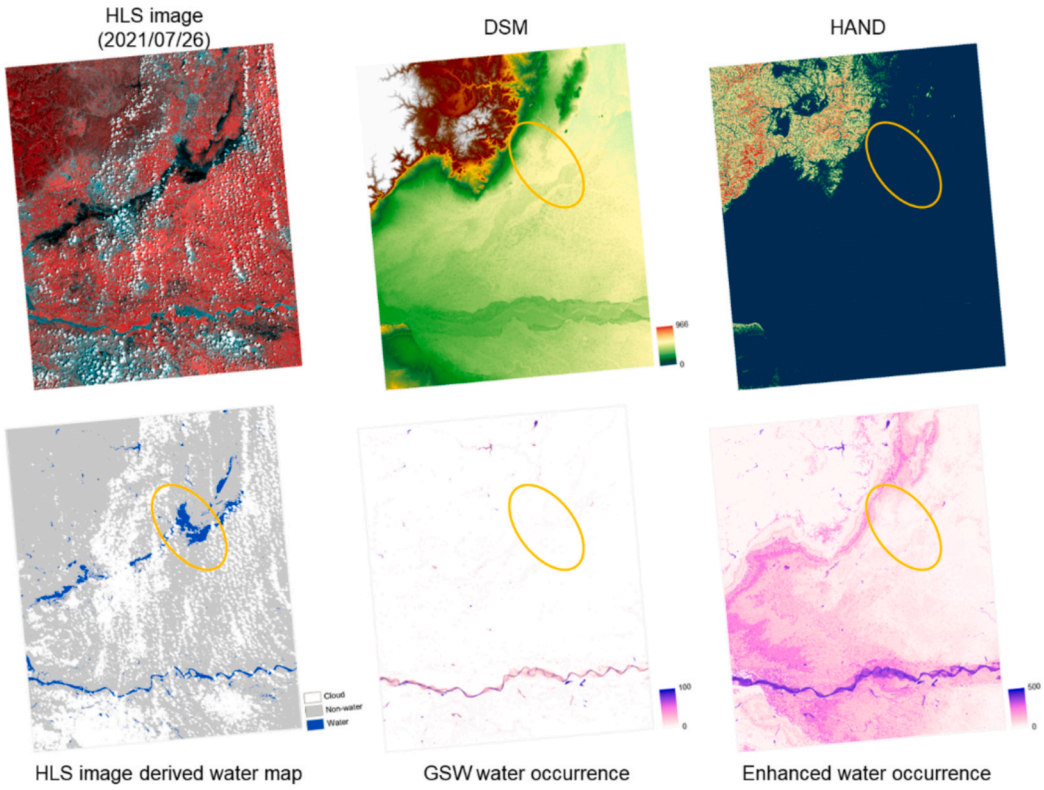

Fig. 6. Limitations of the enhanced water occurrence data generated using the proposed method due to the resolution and quality constraints of the DSM data. This example is taken from a local area affected by the 2021 flood event in Xinxiang City, Henan Province, China, where satellite-observed inundation areas were not consistent with inundation probabilities indicated by the enhanced water occurrence data.

improving seamless flood mapping. It also discusses the complementary potential of SAR-optical data fusion approaches, especially under persistent cloud cover. Additionally, this study confirmed the value of applying cloud reconstruction to flood mapping with optical satellite imagery, emphasizing its importance in reducing cloud cover effects in composed flood maps such as flood duration maps. However, the identified limitations of the proposed method suggest the necessity for high-resolution terrain data to further reduce uncertainties in reconstructed seamless flood maps.

Moreover, future research could explore the integration of satellite, airborne, and in-situ observations to enhance the accuracy and spatial detail of flood mapping in complex terrains or urbanized regions. In addition, future efforts should focus on enhancing the fusion process by incorporating local hydro-physical processes to better account for deviations from terrain-based flood susceptibility patterns, thereby improving seamless flood mapping capability in the context of increasingly severe flood risks.

CRediT authorship contribution statement

Zhiwei Li: Writing – review & editing, Writing – original draft, Visualization, Validation, Supervision, Resources, Methodology, Investigation, Funding acquisition, Conceptualization. **Shaofen Xu:** Writing – original draft, Visualization, Validation, Software, Resources, Methodology, Investigation, Formal analysis, Data curation. **Qihao Weng:** Writing – review & editing, Supervision, Project administration, Funding acquisition, Conceptualization.

Declaration of competing interest

The authors declare the following financial interests/personal relationships which may be considered as potential competing interests: Qihao Weng reports financial support was provided by Global STEM Professorship. Qihao Weng reports financial support was provided by The Hong Kong Polytechnic University. Zhiwei Li reports financial support was provided by National Natural Science Foundation of China. If there are other authors, they declare that they have no known competing financial interests or personal relationships that could have appeared to influence the work reported in this paper.

Acknowledgments

This study was funded by the Global STEM Professorship (P0039329), The Hong Kong Polytechnic University (P0046482, P0038446, and P0042484), and the National Natural Science Foundation of China (No. 42101357). The authors gratefully acknowledge Planet Labs for providing access to PlanetScope imagery used in this study.

Appendix A. Supplementary data

Supplementary data to this article can be found online at https://doi.org/10.1016/j.jag.2025.104855.

Data availability

Data will be made available on request.

References

Albanwan, H., Qin, R., Tang, Y., 2024. Image fusion in remote sensing: An overview and meta-analysis. Photogramm. Eng. Remote Sens. 90, 755–775. https://doi.org/10.14358/PERS.24-00110R1.

Bai, B., Tan, Y., Donchyts, G., Haag, A., Xu, B., Chen, G., Weerts, A.H., 2023. Naive Bayes classification-based surface water gap-filling from partially contaminated optical remote sensing image. J. Hydrol. 616. https://doi.org/10.1016/j.jhydrol.2022.128791.

Bai, B., Tan, Y., Zhou, K., Donchyts, G., Haag, A., Weerts, A.H., 2022. Time-series surface water gap filling based on spatiotemporal neighbourhood similarity. Int. J. Appl. Earth Obs. Geoinf. 112, 102882. https://doi.org/10.1016/j.jag.2022.102882.

Bofana, J., Zhang, M., Wu, B., Zeng, H., Nabil, M., Zhang, N., Elnashar, A., Tian, F., da Silva, J.M., Botão, A., Atumane, A., Mushore, T.D., Yan, N., 2022. How long did crops survive from floods caused by Cyclone Idai in Mozambique detected with multi-satellite data. Remote Sens. Environ. 269, 112808. https://doi.org/10.1016/j.rse.2021.112808.

Chen, F., Zhang, M., Zhao, H., Guan, W., Yang, A., 2024. Pakistan's 2022 floods: Spatial distribution, causes and future trends from Sentinel-1 SAR observations. Remote Sens. Environ. 304, 114055. https://doi.org/10.1016/j.rse.2024.114055.

Claverie, M., Ju, J., Masek, J.G., Dungan, J.L., Vermote, E.F., Roger, J.C., Skakun, S.V., Justice, C., 2018. The Harmonized Landsat and Sentinel-2 surface reflectance data set. Remote Sens. Environ. 219, 145–161. https://doi.org/10.1016/j.rse.2018.09.002.

Donchyts, G., Winsemius, H., Schellekens, J., Erickson, T., Gao, H., Savenije, H., van de Giesen, N., 2016. Global 30m Height Above the Nearest Drainage. Presented at the European Geosciences Union, Vienna, Austria. https://doi.org/10.13140/RG.2.1.3956.8880.

Fawakherji, M., Hashemi-Beni, L., 2025. Flood detection and mapping through multi-resolution sensor fusion: integrating UAV optical imagery and satellite SAR data. Geomat. Nat. Haz. Risk 16, 2493225. https://doi.org/10.1080/19475705.2025.2493225.

Feng, L., Pi, X., Luo, Q., Li, W., 2023. Reconstruction of long-term high-resolution lake variability: Algorithm improvement and applications in China. Remote Sens. Environ. 297, 113775. https://doi.org/10.1016/j.rse.2023.113775.

Fichtner, F., Mandery, N., Wieland, M., Groth, S., Martinis, S., Riedlinger, T., 2023. Time-series analysis of Sentinel-1/2 data for flood detection using a discrete global grid system and seasonal decomposition. Int. J. Appl. Earth Obs. Geoinf. 119, 103329. https://doi.org/10.1016/j.jag.2023.103329.

Fraehr, N., Wang, Q.J., Wu, W., Nathan, R., 2023. Supercharging hydrodynamic inundation models for instant flood insight. Nat. Water 1, 835–843. https://doi.org/10.1038/s44221-023-00132-2.

Giustarini, L., Hostache, R., Kavetski, D., Chini, M., Corato, G., Schlaffer, S., Matgen, P., 2016. Probabilistic flood mapping using synthetic aperture radar data. IEEE Trans. Geosci. Remote Sens. 54, 6958–6969. https://doi.org/10.1109/TGRS.2016.2592951.

Goffi, A., Stroppiana, D., Brivio, P.A., Bordogna, G., Boschetti, M., 2020. Towards an automated approach to map flooded areas from Sentinel-2 MSI data and soft integration of water spectral features. Int. J. Appl. Earth Obs. Geoinf. 84, 101951. https://doi.org/10.1016/j.jag.2019.101951.

Hashemi-Beni, L., Gebrehiwot, A.A., 2021. Flood extent mapping: An integrated method using deep learning and region growing using UAV optical data. IEEE J. Sel. Top. Appl. Earth Obs. Remote Sens. 14, 2127–2135. https://doi.org/10.1109/JSTARS.2021.3051873.

Helleis, M., Wieland, M., Krullikowski, C., Martinis, S., Plank, S., 2022. Sentinel-1-based water and flood mapping: benchmarking convolutional neural networks against an operational rule-based processing chain. IEEE J. Sel. Top. Appl. Earth Obs. Remote Sens. 15, 2023–2036. https://doi.org/10.1109/JSTARS.2022.3152127.

Huang, W., Wang, F., Duan, W., Tang, L., Qin, J., Meng, X., 2023. Image similarity-based gap filling method can effectively enrich surface water mapping information. ISPRS J. Photogramm. Remote Sens. 202, 528–544. https://doi.org/10.1016/j.isprsjprs.2023.07.011.

IPCC, 2023. Climate Change 2021 – The Physical Science Basis. Cambridge University Press. https://doi.org/10.1017/9781009157896.

Jakubik, J., Chu, L., Fraccaro, P., Gomes, C., Nyirjesy, G., Bangalore, R., Lambhate, D., Das, K., Oliveira Borges, D., Kimura, D., Simumba, N., Szwarcman, D., Muszynski, M., Weldemariam, K., Zadrozny, B., Ganti, R., Costa, C., Edwards Blair & Watson, C., Mukkavilli, K., Schmude Johannes & Hamann, H., Robert, P., Roy, S., Phillips, C., Ankur, K., Ramasubramanian, M., Gurung, I., Leong, W.J., Avery, R., Ramachandran, R., Maskey, M., Olofossen, P., Fancher, E., Lee, T., Murphy, K., Duffy, D., Little, M., Alemohammad, H., Cecil, M., Li, S., Khallaghi, S., Godwin, D., Ahmadi, M., Kordi, F., Saux, B., Pastick, N., Doucette, P., Fleckenstein, R., Luanga, D., Corvin, A., Granger, E., 2023. Prithvi-100M.https://github.com/NASA-IMPACT/hls-foundation-os. https://doi.org/10.57967/hf/0952.

Konapala, G., Kumar, S.V., Khalique Ahmad, S., 2021. Exploring Sentinel-1 and Sentinel-2 diversity for flood inundation mapping using deep learning. ISPRS J. Photogramm. Remote Sens. 180, 163–173. https://doi.org/10.1016/j.isprsjprs.2021.08.016.

Li, M., Zhao, C., Huang, Q., Pan, T., Yesou, H., Nerry, F., Li, Z.-L., 2025. Combining Landsat 5 TM and UAV images to estimate river discharge with limited ground-based flow velocity and water level observations. Remote Sens. Environ. 318, 114610. https://doi.org/10.1016/j.rse.2025.114610.

Li, X., Ling, F., Foody, G.M., Boyd, D.S., Jiang, L., Zhang, Y., Zhou, P., Wang, Y., Chen, R., Du, Y., 2021a. Monitoring high spatiotemporal water dynamics by fusing MODIS, Landsat, water occurrence data and DEM. Remote Sens. Environ. 265, 112680. https://doi.org/10.1016/j.rse.2021.112680.

Li, X., Ling, F., Cai, X., Ge, Y., Li, X., Yin, Z., Shang, C., Jia, X., Du, Y., 2021b. Mapping water bodies under cloud cover using remotely sensed optical images and a spatiotemporal dependence model. Int. J. Appl. Earth Obs. Geoinf. 103, 102470. https://doi.org/10.1016/j.jag.2021.102470.

Li, Y., Dang, B., Zhang, Y., Du, Z., 2022a. Water body classification from high-resolution optical remote sensing imagery: Achievements and perspectives. ISPRS J. Photogramm. Remote Sens. 187, 306–327. https://doi.org/10.1016/j.isprsjprs.2022.03.013.

Li, Z., Shen, H., Weng, Q., Zhang, Y., Dou, P., Zhang, L., 2022b. Cloud and cloud shadow detection for optical satellite imagery: Features, algorithms, validation, and prospects. ISPRS J. Photogramm. Remote Sens. 188, 89–108. https://doi.org/10.1016/j.isprsjprs.2022.03.020.

Li, Z., Xu, S., Weng, Q., 2024a. Beyond clouds: Seamless flood mapping using Harmonized Landsat and Sentinel-2 time series imagery and water occurrence data. ISPRS J. Photogramm. Remote Sens. 216, 185–199. https://doi.org/10.1016/j.isprsjprs.2024.07.022.

Li, Z., Xu, S., Weng, Q., 2024b. Can We Reconstruct Cloud-Covered Flooding Areas in Harmonized Landsat and Sentinel-2 Image Time Series?, in: IGARSS 2024 - 2024 IEEE International Geoscience and Remote Sensing Symposium. IEEE, pp. 3187–3189. https://doi.org/10.1109/IGARSS53475.2024.10642149.

Li, Z., Yoo, C., Weng, Q., 2024c. Urban Flooding Monitoring and Management in Geospatial Perspective: Data, Techniques, and Platforms, in: Handbook of Geospatial Approaches to Sustainable Cities. CRC Press, pp. 44–57.

Martinis, S., Groth, S., Wieland, M., Knopp, L., Rättich, M., 2022. Towards a global seasonal and permanent reference water product from Sentinel-1/2 data for improved flood mapping. Remote Sens. Environ. 278, 113077. https://doi.org/10.1016/j.rse.2022.113077.

McCormack, T., Campanyà, J., Naughton, O., 2022. A methodology for mapping annual flood extent using multi-temporal Sentinel-1 imagery. Remote Sens. Environ. 282, 113273. https://doi.org/10.1016/j.rse.2022.113273.

Mullen, C., Penny, G., Müller, M.F., 2021. A simple cloud-filling approach for remote sensing water cover assessments. Hydrol. Earth Syst. Sci. 25, 2373–2386. https://doi.org/10.5194/hess-25-2373-2021.

Notti, D., Giordan, D., Caló, F., Pepe, A., Zucca, F., Galve, J.P., 2018. Potential and limitations of open satellite data for flood mapping. Remote Sens. (Basel) 10, 1673. https://doi.org/10.3390/rs10111673.

Pekel, J.-F., Cottam, A., Gorelick, N., Belward, A.S., 2016. High-resolution mapping of global surface water and its long-term changes. Nature 540, 418–422. https://doi.org/10.1038/nature20584.

Peramuna, P.D.P.O., Neluwala, N.G.P.B., Wijesundara, K.K., DeSilva, S., Venkatesan, S., Dissanayake, P.B.R., 2025. Enhancing 2D hydrodynamic flood model predictions in data-scarce regions through integration of multiple terrain datasets. J. Hydrol. 648, 132343. https://doi.org/10.1016/j.jhydrol.2024.132343.

Rentschler, J., Salhab, M., Jafino, B.A., 2022. Flood exposure and poverty in 188 countries. Nat. Commun. 13. https://doi.org/10.1038/s41467-022-30727-4.

Schumann, G., Giustarini, L., Tarpanelli, A., Jarihani, B., Martinis, S., 2022. Flood modeling and prediction using earth observation data. Surv. Geophys. https://doi.org/10.1007/s10712-022-09751-y.

Shastry, A., Carter, E., Coltin, B., Sleeter, R., McMichael, S., Eggleston, J., 2023. Mapping floods from remote sensing data and quantifying the effects of surface obstruction by clouds and vegetation. Remote Sens. Environ. 291, 113556. https://doi.org/10.1016/j.rse.2023.113556.

Tadono, T., Ishida, H., Oda, F., Naito, S., Minakawa, K., Iwamoto, H., 2014. Precise global DEM generation by ALOS PRISM. ISPRS Ann. Photogramm. Remote Sens. Spat. Inf. Sci. II–4, 71–76. https://doi.org/10.5194/isprsannals-II-4-71-2014.

Takaku, J., Tadono, T., Tsutsui, K., 2014. Generation of high resolution global DSM from ALOS PRISM. Int. Arch. Photogramm. Remote. Sens. Spat. Inf. Sci. XL–4, 243–248. https://doi.org/10.5194/isprsarchives-XL-4-243-2014.

Takaku, J., Tadono, T., Tsutsui, K., Ichikawa, M., 2016. Validation of "AW3D" Global DSM generated from ALOS PRISM. ISPRS Ann. Photogramm. Remote Sens. Spat. Inf. Sci. III–4, 25–31. https://doi.org/10.5194/isprs-annals-III-4-25-2016.

Tellman, B., Sullivan, J.A., Kuhn, C., Kettner, A.J., Doyle, C.S., Brakenridge, G.R., Erickson, T.A., Slayback, D.A., 2021. Satellite imaging reveals increased proportion of population exposed to floods. Nature 596, 80–86. https://doi.org/10.1038/s41586-021-03695-w.

Tulbure, M.G., Broich, M., Perin, V., Gaines, M., Ju, J., Stehman, S.V., Pavelsky, T., Masek, J.G., Yin, S., Mai, J., Betbeder-Matibet, L., 2022. Can we detect more ephemeral floods with higher density harmonized Landsat Sentinel 2 data compared to Landsat 8 alone? ISPRS J. Photogramm. Remote Sens. 185, 232–246. https://doi.org/10.1016/j.isprsjprs.2022.01.021.

Tupas, M.E., Roth, F., Bauer-Marschallinger, B., Wagner, W., 2023. Improving sentinel-1 Flood maps using a topographic index as prior in bayesian inference. Water 15, 4034. https://doi.org/10.3390/w15234034.

Vermote, E., Saleous, N., 2007. LEDAPS surface reflectance product description. University of Idots, College Park, pp. 1–21.

Wang, Y., Xin, Z., Zhang, C., Han, P., Pi, X., Song, C., 2024a. Revealing lake dynamics across the Amur River Basin over the past two decades using multi-source remote sensing datasets. J. Hydrol.: Reg. Stud. 55, 101928. https://doi.org/10.1016/j.ejrh.2024.101928.

Wang, Z., Chen, Y., Zeng, Z., Chen, X., Li, X., Jiang, X., Lai, C., 2024. A tight coupling model for urban flood simulation based on SWMM and TELEMAC-2D and the uncertainty analysis. Sustain. Cities Soc. 114, 105794. https://doi.org/10.1016/j.scs.2024.105794.

Xu, Q., Shi, Y., Bamber, J.L., Ouyang, C., Zhu, X.X., 2024. Large-scale flood modeling and forecasting with FloodCast. Water Res. 264, 122162. https://doi.org/10.1016/j.watres.2024.122162.

Yokoya, N., Yamanoi, K., He, W., Baier, G., Adriano, B., Miura, H., Oishi, S., 2022. Breaking limits of remote sensing by deep learning from simulated data for flood and debris-flow mapping. IEEE Trans. Geosci. Remote Sensing 60, 1–15. https://doi.org/10.1109/TGRS.2020.3035469.

Yue, L., Li, B., Zhu, S., Yuan, Q., Shen, H., 2023. A fully automatic and high-accuracy surface water mapping framework on Google Earth Engine using Landsat time-series. Int. J. Digital Earth 16, 210–233. https://doi.org/10.1080/17538947.2023.2166606.

Zhao, G., Gao, H., 2018. Automatic correction of contaminated images for assessment of reservoir surface area dynamics. Geophys. Res. Lett. 45, 6092–6099. https://doi.org/10.1029/2018GL078343.

Zhu, Z., Woodcock, C.E., 2012. Object-based cloud and cloud shadow detection in Landsat imagery. Remote Sens. Environ. 118, 83–94. https://doi.org/10.1016/j.rse.2011.10.028.

Zingaro, M., Hostache, R., Chini, M., Capolongo, D., Matgen, P., 2024. A localized particle filtering approach to advance flood frequency estimation at large scale using satellite synthetic aperture radar image collection and hydrodynamic modelling. Remote Sens. (Basel) 16, 2179. https://doi.org/10.3390/rs16122179.